Integrating Materials and Manufacturing Innovation (2023) 12:493–501
https://doi.org/10.1007/s40192-023-00323-5

TECHNICAL ARTICLE

Laser Powder Bed Fusion Process and Structure Data Set for Process Model Validations

Nathaniel Wood[1] · Edwin Schwalbach[2] · Andrew Gillman[2] · David J. Hoelzle[1]

Received: 15 July 2023 / Accepted: 26 October 2023 / Published online: 13 December 2023
© The Minerals, Metals & Materials Society 2023

Abstract

This work reports the measurement of laser powder bed fusion (PBF) process input signals, output signals, and structural data for a set of eight IN 718 samples. Data from multiple samples imparts statistical replicability to the measurements. The input signals are the real-time PBF laser position commands, power commands, and the beam radius set point. The output signals are thermographic videos from coaxial and off-axis infrared cameras, and temperature measurements from thermocouples embedded in the samples. The structural data are optical micrographs of all built surfaces. Data are collected for three testing regimes: First, the laser rasters over the samples under conditions that do not induce melting. Second, the laser rasters over the samples with conditions that induce melting. Lastly, five layers of IN 718 are built atop the samples. The main result is an open and comprehensive data set, comprising both raw and processed signal data, for validating PBF process and structure models.

Keywords Powder bed fusion · Process validation · Process modeling · Quality control

Introduction

Powder bed fusion (PBF), and in particular, laser PBF of metals, is a class of additive manufacturing processes in which parts with complex geometry can be fabricated from powdered feedstock in a layer-by-layer manner [1]. PBF is poised to have significant industrial impacts over the coming decade; however, the process is currently limited by defects like high levels of residual stresses [2–4], porosity [5–7], and anisotropy in material properties [7–12]. Each of these types of defects are directly related to poor thermal management and thus there is considerable interest in accurate predictive modeling to better understand the relationships between process inputs, geometry, material properties, and temperature history and structure. Despite the wealth of thermal modeling efforts and literature [13–22], which often include validations against data, there are few research efforts that release validation data that is open, comprehensive, complete, and replicated. The data set of this manuscript makes the following contributions:

- *Open* All data are made freely available at [23]. We anticipate that this will be an instrumental data set for the validation and calibration of PBF process and structure models.
- *Comprehensive* Thermal modeling efforts are varied in complexity and dimensional scope, ranging from conductive heat transfer at the part scale [14–16] and melt pool scale [17] to complex multiphysics modeling at the melt pool [18–21] or atomistic scale [22]. Our data set is applicable to validating models across this range for the following reasons:
  - *Physics excited* The experiment tested three different laser power levels: two power levels below the minimum that produces a melt pool, and one power level above this value. In the two former tests, only conductive heat transfer occurred, and in the latter test, the heat transfer encompassed conduction, convection, and phase change. Thus, this data set is important for understanding the tradeoff between model complexity and prediction accuracy.

✉ Nathaniel Wood
wood.863@osu.edu
Edwin Schwalbach
edwin.schwalbach@afrl.af.mil
Andrew Gillman
andrew.gillman.2@afrl.af.mil
David J. Hoelzle
hoelzle.1@osu.edu

[1] Mechanical and Aerospace Engineering, The Ohio State University, Columbus, OH 43210, USA

[2] Materials and Manufacturing Directorate, Air Force Research Laboratory, Dayton, OH 45433-5519, USA

- *Boundary conditions* Two different geometries—one rectangular prism and one with an I-beam cross-section—were tested to impose two different boundary conditions. In contrast, many efforts test single layers [24, 25], rectangular prism geometries [26–28], or thin wall sections for the related directed energy deposition process [29–31]. The complex geometry here created subtle, but important, differences in temperature observations.
- *Measurement scope* The data were collected on an open-architecture PBF machine, providing an unprecedented scope of measurements of process inputs and thermal outputs (Fig. 1). The thermal outputs include both part scale ("off axis") and melt pool scale ("coaxial") infrared (IR) cameras, and temperature measurements from thermocouples (TCs) embedded at four spatial locations within each sample in the part (Fig. 1). Four TCs per sample is an uncommon quantity of measurements in the reported literature. We also include structural data in the form of micrographs of the as-built surfaces of all Samples, which we include to process the output measurements and provide data for PBF structural models.

- *Complete* All recorded data is provided in raw and in time-synchronized and processed form, providing a complete experimental data set for model validation.
- *Replicated* Each experiment had four independent replicates, and two of the thermocouples in each sample were placed symmetrically about the geometry, providing a robust, replicated data set to help understand process variability.

The material scope is limited to IN 718. However, we believe that the data provided herein will have impacts on IN 718 researchers and the PBF modeling community in general, and inspire researchers to pursue similar efforts with other materials. The paper proceeds as follows: section "Experiment description" reviews the experiment set up, procedures, and data storage location and section "Representative results" shows representative data. Section "Conclusions and future work" concludes the paper. Please refer to electronic supplementary material (ESM) for our data processing procedures, MOESM2.pdf, and for example IR camera data. This information includes defining the coordinates of each sample (Section S.1, MOESM2.pdf),

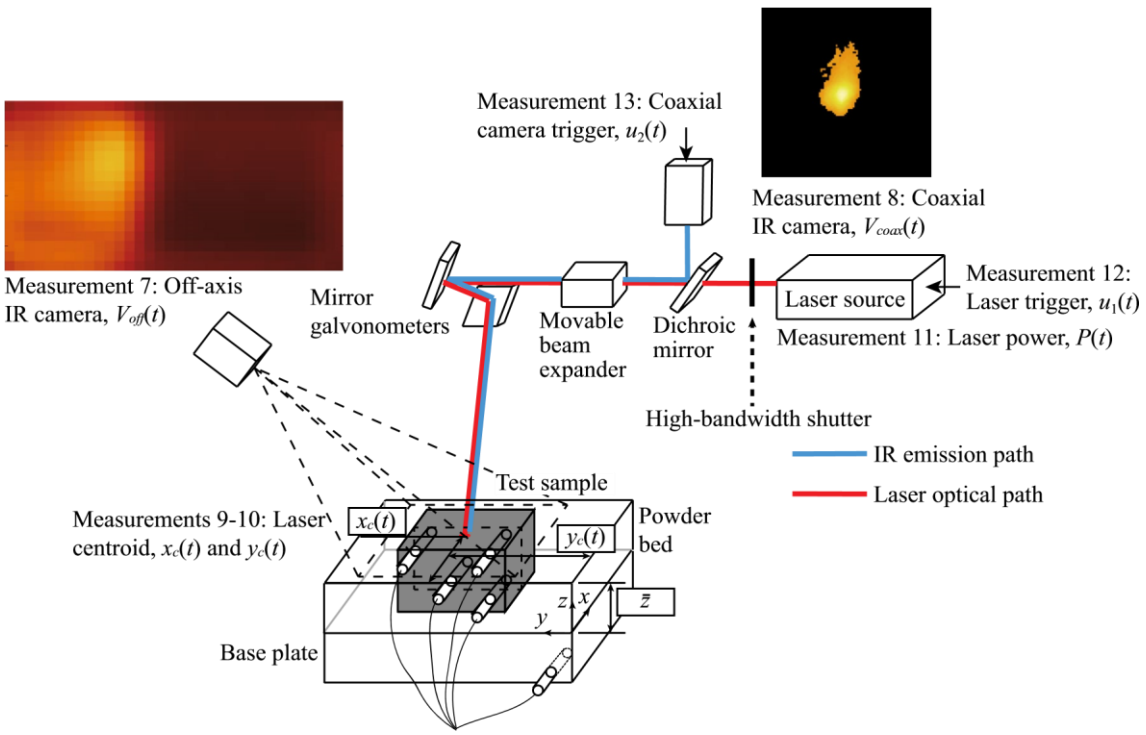

1 3 Measurement 1: Sample stamps, t Measurements 2-6: Embedded thermocouples within test samples ($TCA(t)$, $TCB(t)$, $TCC(t)$, $TCD(t)$) and the base plate ($TC0(t)$)

Fig. 1 Overview of the real-time experimental measurements. Representative images of Measurements 7 and 8 are taken from experimental data

calibrating and processing the IR camera data (Sections S.2 and S.3, MOESM2.pdf), and synchronizing and merging data streams (Sections S.4 and S.5, MOESM2.pdf).

Experiment Description

In this section we describe the configuration of our experimental apparatus, the procedures followed during the experiment, and the organization of all stored data.

Experimental Setup

Machine and Measurements

This experiment was conducted using the open architecture PBF machine owned by Open Additive, LLC, shown here in Fig. 2, a production quality PBF machine with open software tools and modular hardware configuration that is designed for research and development. These features enabled the definition of custom process parameters during the experiment and data collection from all sensors. Control of the machine was accomplished through Open Additive's open machine control software. Low-level communication between modular sensors and synchronized recording of all data streams was controlled by Open Additive's AMSENSE software suite. The schematic of signal collection, including the models of all instruments, is shown in Fig. 4. Our experiment collected the measurements listed below.

- Real-time process outputs

  1. t: Time stamps for all Samples (Measurement 1, Fig. 1).
  2. $TCA(t)$, $TCB(t)$, $TCC(t)$, $TCD(t)$, and $TC0(t)$: Temperature measurements from the 4 TCs embedded within each Sample, denoted TCA, TCB, TCC, and TCD (Measurements 2–5, Fig. 1), and a TC embedded within the base plate, denoted TC0 (Measurement 6, Fig. 1).
  3. $V_{off}(t)$: Thermographic videos of the overall test part taken with an off-axis IR camera (Measurement 7, Fig. 1).
  4. $V_{coax}(t)$: High-resolution thermographic videos of the melt pool taken with a coaxial IR camera (Measurement 8, Fig. 1).

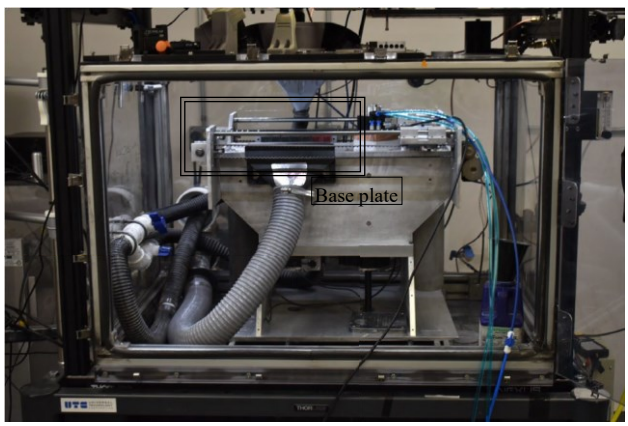

Fig. 2 Open additive PBF machine

- Real-time process inputs

  1. $x_c(t)$ and $y_c(t)$: (x, y) laser position commands sent to the galvonometers (Measurements 9–10, Fig. 1).
  2. $P(t)$: Laser power command (Measurement 11, Fig. 1).
  3. $u_1(t)$ and $u_2(t)$: Binary trigger signals sent to the machine laser source and to the coaxial camera (Measurements 12 and 13, Fig. 1).
  4. Set point for the laser beam diameter used for all Tests (Table 1).

- Post-process part metrology

  1. Measurement 14: Optical micrographs of the Sample top surfaces after Test 3 of (section "Experimental procedures").
  2. Measurement 15: Optical micrographs of single weld tracks to calibrate Measurement 8 of Fig. 1.

Test Samples

Figure 3a–d show the geometry of the test part. The numbering convention for the Samples is shown in Fig. S-2. The Sample design has the following characteristics:

1. *Four spatial locations per part for temperature measurement*: Each Sample had TCs embedded into the four holes shown in Fig. 3c, d, denoted TCA-TCD (Fig. 3e,

Table 1 Process parameters during testing

Parameter	Test			
	1A	1B	2	3 (all layers)
Nominal scan speed, v (mm/s)	1000	1000	1000	1000
Laser spot size, σ (μm)	100	100	100	100
Hatch spacing, h (μm)	100	100	100	100
Overall scan dimensions, (mm × mm)	4×9	4×9	4×9	4×9
Layer thickness, d (μm)	–	–	–	40
Nominal laser power, P_{nom} (W)	42.5	63.75	150	150
Number of sweeps, ^{sw} (–)	3	3	3	1

The test part was machined from IN 718, with the holes for TCA-TCD being manufactured via plunge electrical discharge machining. Engineering drawings of the as-machined dimensions of each Sample, as measured by the machinists, are provided in the electronic supplementary material.

All TCA-TCD holes were fitted with Type K TCs having exposed junctions and IN 600 sheaths (Fig. 4), which were chosen: (1) to match the minimum achievable hole diameter for the depth required and (2) have a time constant (75 ms) that is faster than the heat transfer dynamics at these spatial locations. Figure 3b shows the test part with embedded TCs. TC locations A and B were the minimal feasible distance from the Sample top faces for 0.5 mm diameter, 2.5 mm deep holes, as determined from consultation with machinists.

The base plate and Samples were manufactured separately and bonded with an interference fit. All Sample-base plate and Sample-TC interfaces were coated with Omega OB-600 thermally-conductive cement to ensure good thermal contact.

Data Acquisition (DAQ)

Two DAQs were used by the PBF machine to collect the measurements (Fig. 4). The LabJack DAQ sampled at 1 kHz, which was the intended sample rate of our data set. The

f). These TCs measured temperature near the top surface (A and B), geometric center (C), and near the base plate (D), thus measuring temperature at different scales of magnitude.

2. *Two Sample architectures* Four of the test Samples (Samples 1–4, Fig. 3c) were simple rectangular prisms. Four of the test Samples (Samples 5–8, Fig. 3d) had an I-beam cross-section to study the influence of a complex geometry in PBF heat transfer.
3. *Replicate measurements* Each design was replicated four times to provide four independent measurements. These replicates help assess process variability under identical nominal testing conditions.

FPGA DAQ sampled at its slowest rate of 20 kHz. Our procedures for unifying these data streams are discussed in Section S.4 (MOESM2.pdf).

The laser power delivered to the part surface, $P_{prod}(t)$, was modulated by $P(t)$ and a high bandwidth shutter controlled by $u_1(t)$, which blocked the laser during skywriting. Thus, the power delivered was $P_{prod}(t) = P(t)u_1(t)$. We report the power produced by the source, $P_{prod}(t) = P(t)u_1(t)$, with our processed data, not $P(t)$. Calculation of $P_{prod}(t)$ is in Section S.4 (MOESM2.pdf).

Two IR cameras were used during this experiment: an off-axis camera that imaged the entire test part and a highresolution coaxial melt pool camera. The makes and models of these cameras are given in Fig. 4. The off-axis camera

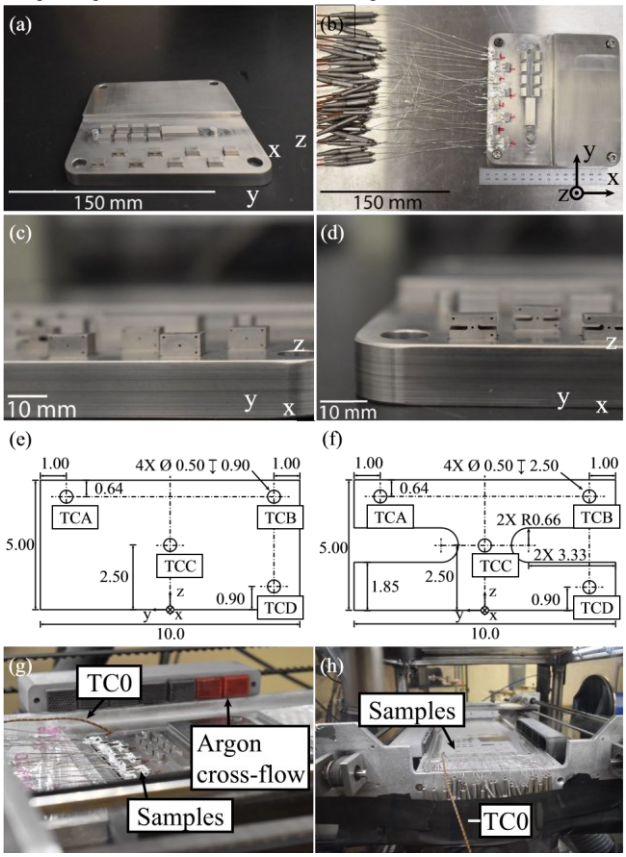

Fig. 3 Test part. **a** Test part layout. Only the foremost eight Samples were instrumented during testing. The remainder of the Samples were for calibration. **b** Test part with Samples instrumented with TCs. The red marks visible on the part denote the machinist's numbering convention, which differs from that used in Fig. S-2. **c** Close-up view of Samples 1–4. **d** Close-up view of Samples 5–8. **e** Engineering drawing of the cross-section of each of Samples 1–4. Units are mm. The out-of-plane depth of the Samples is 5 mm. **f** Engineering drawing of the cross-section of each of Samples 5–8. Units are mm. The out-ofplane depth of the Samples is 5 mm. **g** Configuration of the test part in the PBF machine. Argon cross-flow is along the Sample *y*-axes. **h** Image of the test part in the PBF machine after the addition of powder, Test 3

sampled at 32 Hz and the coaxial camera sampled at 1 kHz. The ESM (MOESM2.pdf) explains how the data from these cameras, $V_{\text{off}}(t)$ and $V_{\text{coax}}(t)$ (Measurements 7 and 8), respectively, were processed and synthesized together.

Experimental Procedures

Table 1 lists the process parameters used during all Tests. Parameters labeled "nominal" describe aspects of the scan which changed over time like the real-time laser speed, which accelerated and decelerated while scanning. The "sweeps" mentioned in Table 1 refer to the scan strategy shown in Fig. 5. Tests 1 and 2 featured 3 sweeps to capture artifacts of turnarounds in the scan strategy, and Test 3 featured only 1 sweep because that single sweep fused the powder. All tests were conducted with a Gaussian-distributed laser beam and in an Argon environment with crossflow in the y-direction (Fig. 3g, h). As discussed in section "Introduction", this experiment comprised three Tests:

Test 1: Raster the laser over the Sample top faces at 42.5 and 63.75 W, sequentially, which we denote as Tests 1A and 1B, respectively. These were 50 and 75% of the smallest power that produces a stable melt pool, which we determined experimentally was 85 W. As mentioned in section "Introduction", conduction was the only mode of heat transfer we intended to provoke during this Test.

Test 2: Raster the laser over the Sample top faces at 150 W without fusion of powder. As mentioned in section "Introduction", this Test added phase change and convection to the heat transfer.

Test 3: Build five new layers of material on the Sample top faces using the 150 W laser from Test 2. This Test added material addition to the heat transfer and mimics all the physics of the commercial process.

Tests 1–3 were performed on each Sample in sequence before brushing off excess powder from untested samples and moving to the next. The locations of the 4 mm × 9 mm bounds of each scan, hereafter called the "scan footprints," were determined manually by the machine technician and were located in the machine coordinates using Measurement 14 of section "Machine and measurements" (Section S.1.2, MOESM2.pdf). Figure S-2 displays these locations.

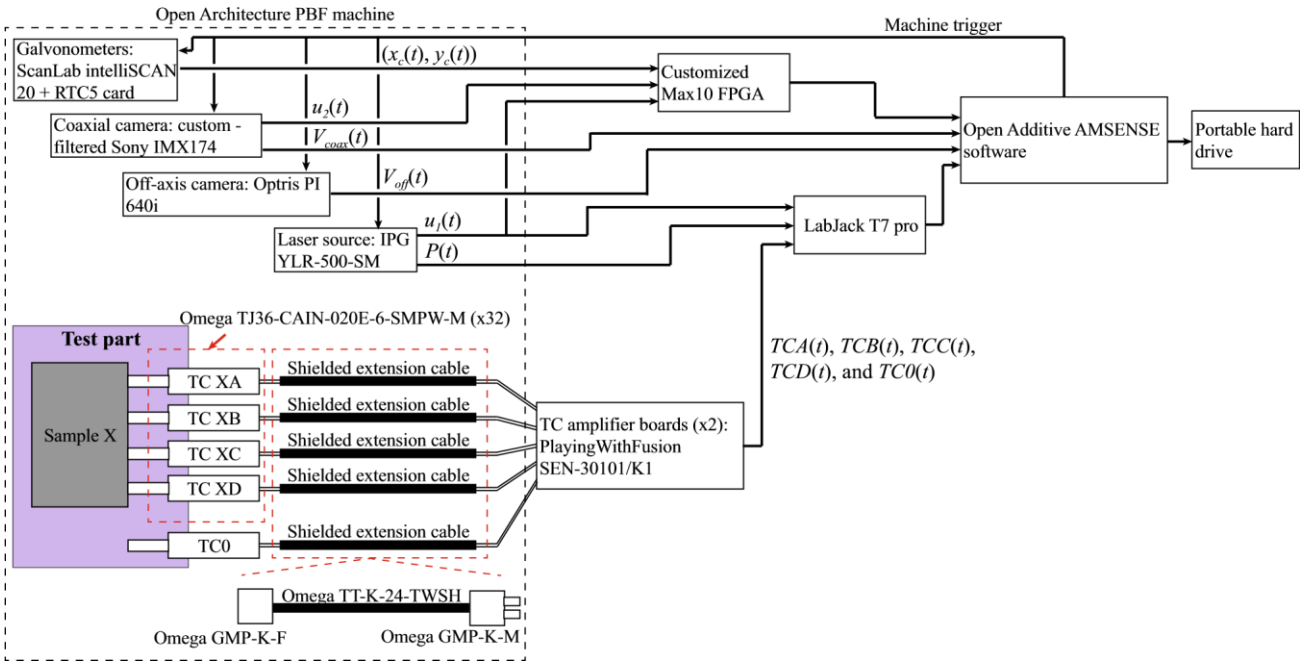

Fig. 4 Schematic of the instruments and signal pathways used in the experiment

Data Storage

The data [23] are hosted on the Materials Data Facility [32]. Both raw and processed data are available (MOESM2.pdf). For the post-process part metrology (Measurements 14 and 15, Sections S.1.1–S.1.2 of MOESM2.pdf), the data comprises individual images and images of the calibration rules. For the real-time process input and output data (Measurements 1–12, section "Experimental procedures"), the data is supplied as both a collection of.csv files and a `MATLAB`. mat file. In the processed data, Measurement 11, $P(t)$, is replaced by $P_{prod}(t)$ of section "Data acquisition (DAQ)". The processed data also includes the locations of all pixels of both cameras at all time steps.

Representative Results

Here, we provide representative results of the experimental data after being processed according to MOESM2.pdf.

We focus on the TC data (Measurements 2–5) and $V_{coax}(t)$ (Measurement 8) in order to showcase the most

informationrich output signals. The electronic supplemental material includes videos of both raw and processed data for both IR cameras.

Table 2 Matrix of camera and TC data status

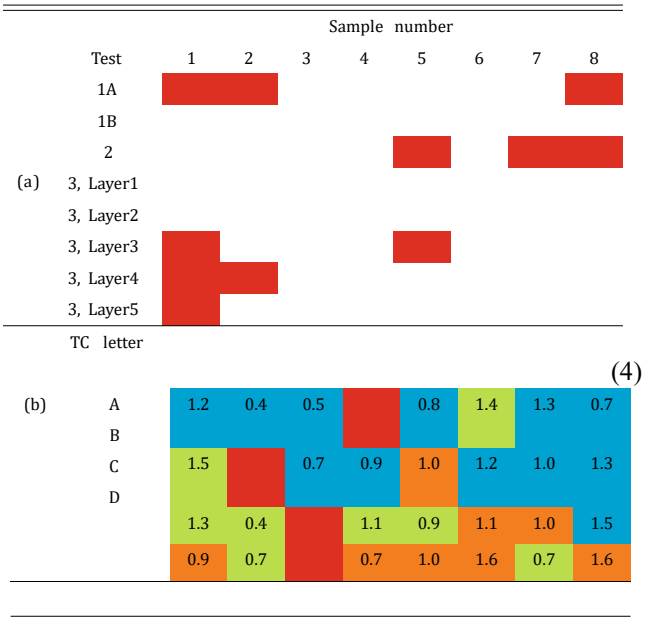

(a) Camera data status, per Test. Filled-in entries denote instances of corrupt data. (b) TC integrity status, per Sample. Red entries denote instances of TCs becoming dislodged or unusable during testing. Otherwise, the numbers in each entry denote the experimentallymeasured depth to which each TC was inserted, in units mm. The cell colors correspond to different measuring techniques, which are discussed in Section S.1.3 of MOESM2.pdf and are as follows: Blue entries denote measurement by method 1. Green entries denote measurement by method 2. Orange entries denote measurement by method 3

TCs 3C, 3D, and 4A were dislodged during assembly and their data lost. Table 2b quantifies other instances of lost TC data via the procedures of Section S.1.3 (MOESM2. pdf). Figure 6 shows the TC data for all Samples in Test 1B, which we chose because none of the 8 Samples lost IR data. Four trends are observable in this figure, which also hold for all other data records.

(1) Temperatures measured by TCA and TCB are the hot- test because these TCs were embedded closest to the top surface, and thus the lasing surface. Similarly, TCD and TC0 measured temperatures that were mostly constant and coolest because they were the farthest from the lasing surface.

(2) Two peaks are visible in the TCA data, and one peak is visible in TCB data. This is because of the scan path shown in Fig. 5, wherein the overall scan direction passed over TCA twice. Likewise, the laser passed over TCB once, effectively, as the temporal difference between laser sweeps in the x-direction was only 24 ms.

(3) The TCC and TCD data for Samples 5–8 are hotter, and colder, respectively, than those for Samples 1–4. This result is expected because the flanges in Samples 5–8 (Fig. 3f) are heat islands. In Samples 5–8, heat predominantly flowed through the TCC position instead of directly from the TCA to TCD positions, which produced elevated TCC data in Samples 5–8 relative to Samples 1–4. Moreover, this restricted heat flow to TCD produced lowered TCD data in Samples 5–8 relative to Samples 1–4.

There is no trend in the TCA and TCB data with respect to Sample number. This result runs contrary to intuition since the TCA and TCB locations are in the flanges of Samples 5–8, therefore one expects the temperatures to be greater for the TCs embedded those Samples. Since TCA and TCB measured temperatures near the melt pool, we corroborate the incongruous TCA and TCB results by investigating the role of part geometry on the melt pool characteristics visible in $V_{coax}(t)$. Figure 7 plots the average peak melt pool temperature

(Fig. 7a), $\bar{T}_{max}$, and average melt pool area (Fig. 7b), $\bar{A}$, with respect to both Test number and Sample number. Since Tests 1 and 2 featured sw = 3 (Table 1) and Test 3 featured sw = 1 , only data from the first sweep for Tests 1 and 2 was considered. We discuss the following two trends:

(4a) For all Samples, both $\bar{T}_{max}$ and $\bar{A}$ dramatically increase in the progression from Test 1 to Test 2, and then decrease throughout Test 3. The increase from Test 1 to Test 2 is expected, since this corresponds to increasing P_{nom} from 42.5 to 63.75 W to 150 W over the same surfaces of bare metal. Tests 2 and 3 use the same 150 W power, however, in Test 3, the laser fused powder atop the surfaces and not the bare metal itself. Figure 7a, b indicate that the powder requires more energy to fuse than the bare metal, since $\bar{T}_{max}$ and $\bar{A}$ decrease between Tests 2 and 3. This is because powder generally has a lower effective thermal conductivity than bare metal [33].

(4b) With the exception of Sample 6, there is no trend in the responses of $\bar{T}_{max}$ and $\bar{A}$ with respect to Sample number. This result indicates that the change in geometry from Samples 1–4 to Samples 5–8 had a negligible effect on the melt pool characteristics,

which corroborates the trend in the TCA and TCB measurements (Fig. 6). We further investigate this trend in Fig. 7c, d. As stated previously, for Samples 5–8, the cross sectional geometry features two distinct

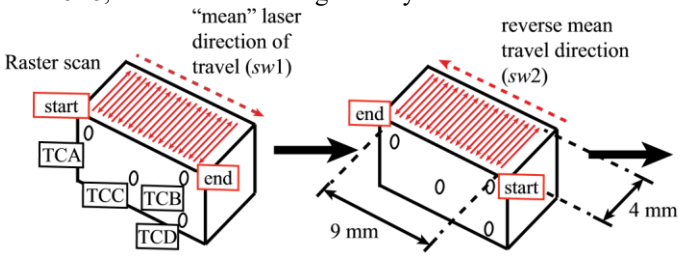

regions (Fig. 3f): the Sample neck in the range $|y| < 0.66$ mm, and the Sample flanges in the range $|y| \in [1.32,5]$ mm, which act as heat islands. We quantify the influence of the flanges on the melt pool characteristics by defining $\Delta\bar{T}_{max} = \bar{T}_{max,flange} - \bar{T}_{max,neck}$ and

$\Delta\bar{A} = \bar{A}_{flange} - \bar{A}_{neck}$, where $\bar{T}_{max,flange}$ and $\bar{A}_{flange}$ are $\bar{T}_{max}$ and $\bar{A}$ for all $\mathbf{y}_c(t)$ (Measurement 10) in

Fig. 5 Laser scan path used during testing

the flanges, and $\bar{T}_{max,neck}$ and $\bar{A}_{neck}$ are $\bar{T}_{max}$ and $\bar{A}$ for all $\mathbf{y}_c(t)$ in the neck. Figure 7c, d plot $\Delta\bar{T}_{max}$ and $\Delta\bar{A}$, which show that no trends exist with respect to Sample number, except $\Delta\bar{A}$ of Sample 6. This results refutes the expectation that the heat islands of Samples 5–8 would distort the melt pool and produce greater $\Delta\bar{T}_{max}$ and $\Delta\bar{A}$ than Samples 1–4. Rather, Fig. 7c, d show that there is consistent nonzero $\Delta\bar{T}_{max}$ and $\Delta\bar{A}$ for Samples 1–4. We conjecture that this effect is from the insulating powder contacting the surfaces at the Sample y-limits, which lay in the flanges. In contrast, the temperatures in the Sample necks were only perturbed by insulating powder at the x-limits, therefore the powder at the y-limits constructed a heat island effect for both geometries.

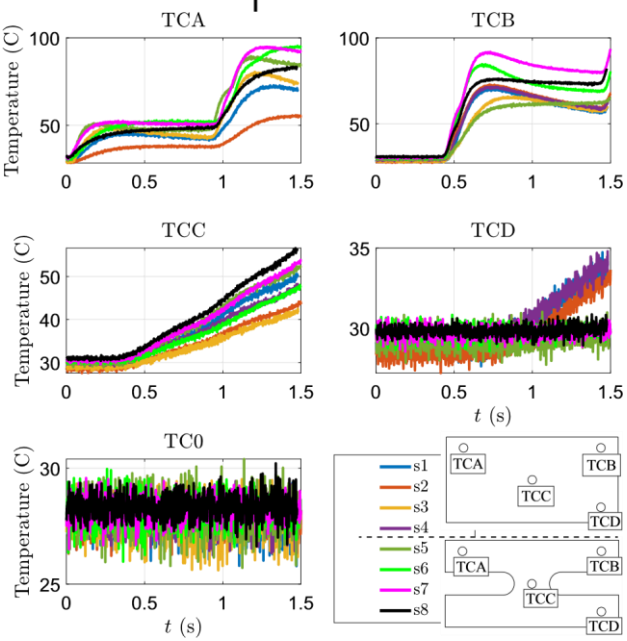

Fig. 6 TC data for all samples in Test 1B, processed according to Section S.4, MOESM2.pdf. Here, "s1"–"s8" abbreviate sample 1 through sample 8

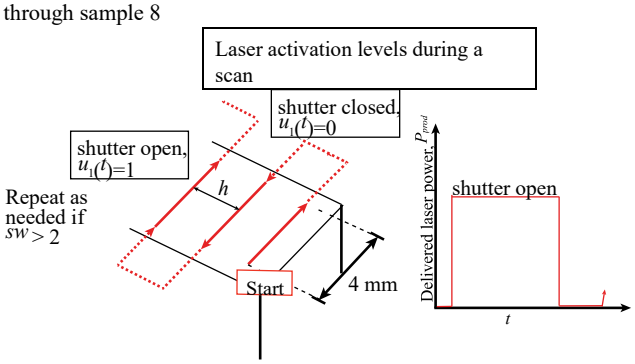

This effect persisted independently of sw, P_{nom}, or layers of fused material, which explains why $\Delta\bar{T}_{max} > 0$ and $\Delta\bar{A} > 0$ for all tests (Fig. 7c, d) and

why no trend with respect to sample number is present in the TCA and TCB data. Only as the temperature field homogenized with decreasing z could this effect diminish enough for geometryinduced perturbances to dominate.

Conclusions and Future Work

This work describes an experiment for gathering an open, comprehensive, complete, and replicated PBF data set of process input, output, and structure measurements for use in validating PBF thermal models of widely varying complexity. The material used in this study was IN718. Eight Samples—machined to mimic partially-completed PBF builds and each instrumented with four embedded thermocouples (TCs)—were subjected to three regimes of tests that induced (1) solely heat conduction in the Samples, (2) conduction, convection, and phase change in the Samples, and (3) all previous heat transfer modes and fusion of powder atop the Samples. During testing, we collected PBF process input signals like the real-time laser power and beam location, output signals like IR camera videos and the TC measurements, and structure data in the form of optical micrographs of the as-built sample surfaces. All raw and processed data (MOESM2.pdf) are made freely available [23].

The scope of the measurements and testing conditions in this data set allows PBF process models to be validated against multiple sources of perturbation. For example, our preliminary analysis of the TC data and IR camera (Figs. 6 and 7) data quantifies how the output measurements correlate with the localized insulation effect of the powder as a function of changing process physics (testing regime) and boundary conditions (sample geometry), while considering process uncertainty like deviations in outputs and TC depth through experimental replicates. We envision this data set being used to validate model predictions of these same outputs under a similarly multivariate analysis. Furthermore, we envision the micrographs of our data set assisting coupled validations of PBF thermal and solidification models. Our data is available in both raw and processed form to facilitate development of new feature extraction techniques from the measurements. To our knowledge, no existing publicly-available data set of the PBF process offers a similar level of comprehensiveness.

Future work includes the characterization of microstructural features of the built material on each Sample via electron backscatter diffraction (EBSD) analysis. We will perform EBSD analysis in 2D on cross-sections of three Samples of each geometry, and reconstruct 3D microstructural fields from a sequence of 2D EBSD images of one sample from each geometry [34]. This data will be made freely available in a subsequent publication, which will help researchers validate models that correlate thermal history with microstructural evolution in 2D and 3D. This is crucial to the mature development of process–structure–properties PBF models and complete digital twins of the process. We also intend to leverage this data set in future works that validate our own PBF process models, which have been tested in simulation [35, 36].

Supplementary Information The online version contains supplementary material available at https://d oi.org/1 0 .1007 /s 40192-023-0 0323- 5.

Acknowledgements The authors acknowledge Patrick Tosh for his help in arranging the experiment, John Middendorf for his help in overseeing the Open Architecture machine, Sean Donegan for his valuable insight in planning the experiment and processing the data, and Abdalla Nassar and David Corbin for assistance with converting.ct5 file calibration data.

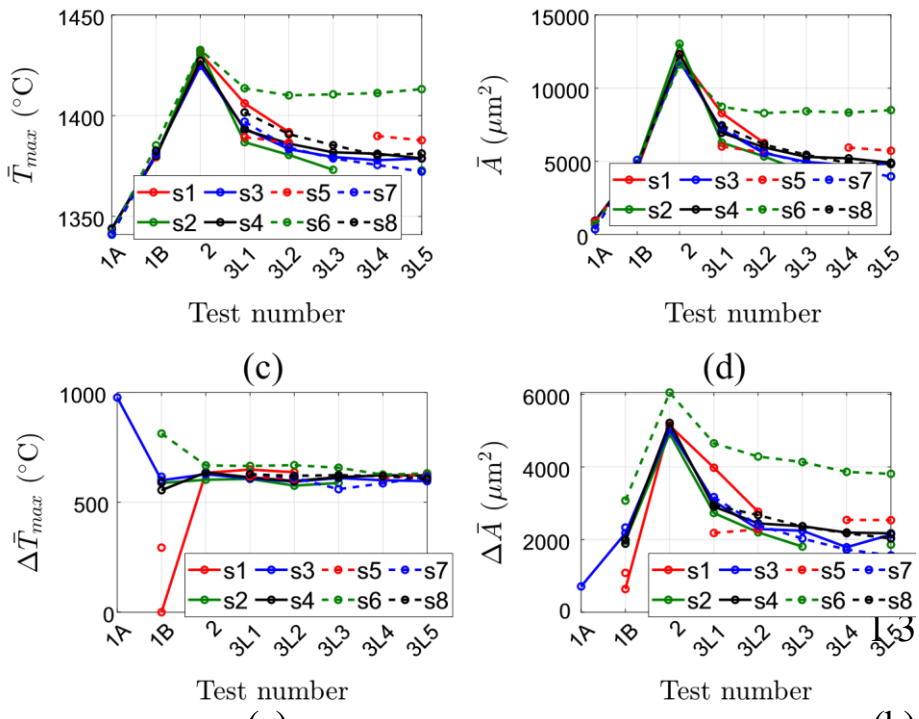

Fig. 7 Analysis of $V_{coax}(t)$ (Measurement 8) here, "s1"–"s8" abbreviate Sample 1 through Sample 8. For data from Tests 1 and 2, only the first sweep of the laser is considered, since Test 3 featured $s = 1$. **a** $\bar{T}_{max}$ for all Samples and Tests. **b** $\bar{A}$ for all Samples and Tests. **c** $\Delta\bar{T}_{max}$ for all Samples and Tests. **d** $\Delta\bar{A}$ for all Samples and Tests

Funding Financial support was provided by the Air Force Research Laboratory under C.N. RX9-OSU-20-5-AFRL2, by the member organizations of the Smart Vehicle Concepts Center, a Phase III National Science Foundation Industry-University Cooperative Research Center (www.S martVehicl eCe nter.o r g) under grant NSF IIP 1738723, and by the NSF Engineering Research Center for Hybrid Autonomous Manufacturing Moving from Evolution to Revolution (ERC-HAMMER) under Award Number EEC-2133630.

Declarations

Conflict of interest On behalf of all authors, the corresponding author states that there is no conflict of interest.

References

1. King WE, Anderson AT, Ferencz RM, Hodge NE, Kamath C, Khairallah SA, Rubenchik AM (2015) Laser powder bed fusion additive manufacturing of metals; physics, computational, and materials challenges. Appl Phys Rev 2(4):041304
2. Peng H, Ghasri-Khouzani M, Gong S, Attardo R, Ostiguy P, Gatrell BA, Budzinski J, Tomonto C, Neidig J, Shankar MR, Billo R, Go DB, Hoelzle D (2018) Fast prediction of thermal distortion in metal powder bed fusion additive manufacturing: Part 1, a thermal circuit network model. Addit Manuf 22:852–868
3. Peng H, Ghasri-Khouzani M, Gong S, Attardo R, Ostiguy P, Gatrell BA, Budzinski J, Tomonto C, Neidig J, Shankar MR, Billo R, Go DB, Hoelzle D (2018) Fast prediction of thermal distortion in metal powder bed fusion additive manufacturing: Part 2, a quasi-static thermo-mechanical model. Addit Manuf 22:869–882
4. Krol TA, Seidel C, Schilp J, Hofmann M, Gan W, Zaeh MF (2013) Verification of structural simulation results of metal-based additive manufacturing by means of neutron diffraction. Phys Procedia
41:849–857
5. Gokuldoss PK, Kolla S, Eckert J (2017) Additive manufacturing processes: selective laser melting, electron beam melting and binder jetting—selection guidelines. Materials (Basel) 10(6):672
6. DebRoy T, Wei HL, Zuback JS, Mukherjee T, Elmer JW, Milewski JO, Beese AM, Wilson-Heid A, De A, Zhang W (2017) Additive manufacturing of metallic components—process, structure and properties. Prog Mater Sci 62:112–224
7. Mower TM, Long MJ (2016) Mechanical behavior of additive manufactured, powder-bed laser-fused materials. Mater Sci Eng A 651:198–213
8. Keist JS, Palmer TA (2016) Role of geometry on properties of additively manufactured Ti–6Al–4V structures fabricated using laser based directed energy deposition. Mater Des 106:482–494
9. Wang T, Zhu YY, Zhang SQ, Wand HM (2015) Grain morphology evolution behavior of titanium alloy components during laser melting deposition additive manufacturing. J Alloy Compd
632:505–513
10. Wei HL, Elmer JW, DebRoy T (2016) Origin of grain orientation during solidification of an aluminum alloy. Acta Mater 115:123–131
11. Yadollahi A, Shamsaei N, Thompson SM, Seely DW (2015) Effects of process time interval and heat treatment on the mechanical and microstructural properties of direct laser deposited 316L stainless steel. Mater Sci Eng A 644:171–183
12. Parimi LL, Ravi GA, Clark D, Attallah MM (2014) Microstructural and texture development in direct laser fabricated IN718. Mater Charact 89:102–111
13. Wei HL, Mukherjee T, Zhang W, Zuback JS, Knapp GL, De A, DebRoy T (2021) Mechanistic models for additive manufacturing of metallic components. Prog Mater Sci 116:100703
14. Yavari R, Williams R, Riensche A, Hooper PA, Cole KD, Jacquemetton L, Halliday HS, Rao PK (2021) Thermal modeling in metal additive manufacturing using graph theory—application to laser powder bed fusion of a large volume impeller. Addit Manuf 41:101956
15. Dugast F, Apostolou P, Fernandez A, Dong W, Chen Q, Strayer S, Wicker R, To AC (2021) Part-scale thermal process modeling for laser powder bed fusion with matrix-free method and GPU computing. Addit Manuf 37:101732
16. Schwalbach EJ, Donegan SP, Chapman MG, Chaput KJ, Groeber MA (2019) A discrete source model of powder bed fusion additive manufacturing thermal history. Addit Manuf 25:485–498
17. Zhang Z, Huang Y, Kasinathan AR, Shahabad SI, Ali U, Mahmoodkhani Y, Toyserkani E (2019) 3-dimensional heat transfer modeling for laser powder-bed fusion additive manufacturing with volumetric heat sources based on varied thermal conductivity and absorptivity. Opt Laser Technol 109:297–312
18. Khairallah SA, Anderson AT, Rubenchik A, King WE (2016) Laser powder-bed fusion additive manufacturing: physics of complex melt flow and formation mechanisms of pores, spatter, and denudation zones. Acta Mater 108:36–45
19. Mukherjee T, Manvatkar V, De A, DebRoy T (2017) Dimensionless numbers in additive manufacturing. J Appl Phys 121(6):064904
20. Khairallah SA, Martin AA, Lee JRI, Guss G, Calta NP, Hammons JA, Nielsen MH, Chaput K, Schwalbach E, Shah MN, Chapman MG, Willey TM, Rubenchik AM, Anderson AT, Wang YM, Matthews MJ, King WE (2020) Controlling interdependent mesonanosecond dynamics and defect generation in metal 3D printing.
Science 368(6491):660–665
21. Zhang Y, Zhang J (2019) Modeling of solidification microstructure evolution in laser powder bed fusion fabricated 316L stainless steel using combined computational fluid dynamics and cellular automata. Addit Manuf 28:750–765
22. Wang Y, Zhou X (2022) Molecular dynamics simulation of Febased metal powder oxidation during laser powder bed fusion. Materials 15(18):6394
23. Wood N, Schwalbach E, Gillman A, Hoelzle DJ (2023) Laser powder bed fusion process and structure data set, spring 2022. Accessed 2023/11/06 10:22:15 https:// doi. org/ 10. 18126/ JV0R- CYU9
24. Denlinger ER, Jagdale V, Srinivasan GV, El-Wardany T, Michaleris P (2016) Thermal modeling of Inconel 718 processed with powder bed fusion and experimental validation using in situ measurements. Addit Manuf 11:7–15
25. Kolossov S, Boillat E, Glardon R, Fischer P, Locher M (2004) 3D FE simulation for temperature evolution in the selective laser sintering process. Int J Mach Tools Manuf 44:117–123
26. Roberts IA, Wang CJ, Esterlein R, Stanford M, Mynors DJ (2009) A three-dimensional finite element analysis of the temperature field during laser melting of metal powders in additive layer manufacturing. Int J Mach Tools Manuf 49:916–923
27. Denlinger ER, Gouge M, Irwin J, Michaleris P (2017) Thermomechanical model development and in situ experimental

validation of the laser powder-bed fusion process. Addit Manuf 16:73–80
28. Dunbar AJ, Denlinger ER, Heigel J, Michaleris P, Guerrier P, Martukanitz R, Simpson TW (2016) Development of experimental method of in situ distortion and temperature measurements during the laser powder bed fusion additive manufacturing process. Addit Manuf 12:25–30
29. Peyre P, Aubry P, Fabbro R, Neveu R, Longuet A (2008) Analytical and numerical modeling of the direct metal deposition laser process. J Phys D Appl Phys 41:025403
30. Plati A, Tan JC, Golosnoy O, Persoons R, Acker K, Clyne TW (2006) Residual stress generation during laser cladding of steel with a particulate metal matrix composite. Adv Eng Mater 8:619–624
31. Heigel JC, Michaleris P, Reutzel EW (2015) Thermo-mechanical model development and validation of directed energy deposition additive manufacturing of Ti–6Al–4V. Addit Manuf 5:9–19
32. Blaiszik B, Chard K, Pruyne J, Ananthakrishnan R, Tuecke S, Foster I (2016) The materials data facility: data services to advance materials science research. JOM 68(8):2045–2052
33. Zhang S, Lane B, Whiting J, Chou K (2019) On thermal properties of metallic powder in laser powder bed fusion additive manufacturing. J Manuf Process 47:382–392
34. Chapman MG, Shah MN, Donegan SP, Scott JM, Shade PA, Menasche D, Uchic MD (2021) AFRL additive manufacturing modeling series: challenge 4, 3D reconstruction of an IN625 highenergy diffraction microscopy sample using multi-modal serial sectioning. Integr Mater Manuf Innov 10:129–141
35. Wood N, Schwalbach E, Gillman A, Hoelzle DJ (2021) The ensemble Kalman filter as a tool for estimating temperatures in the powder bed fusion process. In: American control conference 2021, New Orleans, LA, USA, pp 4369–4375
36. Wood N, Schwalbach E, Gillman A, Hoelzle DJ (2021) On the diminishing returns of thermal camera resolution for PBF temperature estimation. In: 2021 International solid freeform fabrication symposium, Austin, TX, 2021, pp 319–338

Springer Nature or its licensor (e.g. a society or other partner) holds exclusive rights to this article under a publishing agreement with the author(s) or other rightsholder(s); author self-archiving of the accepted manuscript version of this article is solely governed by the terms of such publishing agreement and applicable law.